

COMPLETE MODE SPECTRUM OF A GROUNDED DIELECTRIC SLAB WITH DOUBLE NEGATIVE METAMATERIALS

W. Shu and J. M. Song

Iowa State University
2215 Coover Hall, Ames, IA 50011, USA

Abstract—The properties of a grounded dielectric slab with double negative (DNG) metamaterials are investigated in this paper. Dramatically different dispersion curves of evanescent surface modes (electromagnetic fields exponentially decay both in air and inside the slab) are observed. They are highly dependent on the medium parameters. As the counterpart of the improper complex leaky modes in a double positive (DPS) medium, the complex modes in a DNG medium are proved to be exclusively proper. They have exponentially decaying fields in the air region and are termed complex surface modes. It is found that there are an infinite number of complex surface modes and they cannot be suppressed. The Poynting vectors of complex surface modes are studied and it is proved that their integrals along the transverse direction are simply zero. The complete mode spectrum of the dielectric slab for both DPS and DNG media are tabled and compared. Surface wave suppression is discussed and its necessary and sufficient conditions are presented.

1. INTRODUCTION

Double negative (DNG) metamaterials have attracted intensive interest in the last few years for their exotic properties, such as negative refraction, reversed Doppler effect, reversed Vavilov-Cerenkov effect, and the possibility of making perfect lens [1–14]. Theoretical investigations and practical experiments are being well undergone by many research groups over the world. Applications are found in RF circuit design [11, 12], antenna size reduction [13, 14], resonance devices [9, 10], *etc.*

The guided dielectric slab with a DNG medium has been studied by several groups. [15] and [16] found that there are special regions

for TM (transverse magnetic) modes where two different propagation constants exist. [17] theoretically investigated the properties of a planar two-layered waveguide, whose one layer is a double positive (DPS) medium and the other is a DNG medium. Super slow-waves with extremely short wavelengths were found whose fields exponentially decay from the interface of the two slabs inside both layers. These guided modes, termed as evanescent surface modes, were also found by [18] and [19], respectively. The graphical solutions of the real modes were reported in [20], but the evanescent surface mode was missed. The grounded dielectric slab also supports complex modes even for lossless media [21, 22]. P. Baccarelli and his colleagues proposed the concept of surface wave suppression, which ensures the absence of both ordinary and evanescent surface modes. This is very attractive in view of taking the DNG medium as a potential substrate candidate to reduce edge diffraction effects and enhance radiation efficiency for microstrip antennas [23, 24].

In this paper, the authors focus on the properties of the evanescent surface modes and the complex modes of the DNG media, both of which belong to the proper mode spectrum. The evanescent surface modes have exponentially decreasing fields in both air and dielectric layer. Their dispersion curves can be dramatically different when with different media parameters. Besides evanescent surface modes, complex modes are found to be with a DNG medium. In Appendix A, it is proved that the complex modes are exclusively proper and thus they are termed complex surface modes. The complex surface modes have high cutoff frequencies which means they exist only when the frequency is lower than their respective cutoff frequencies. This property implies two facts: an infinite number of complex surface modes exist at any frequency and they cannot be suppressed. The investigation on the Poynting vectors shows that their integral results along the longitudinal directions are zero [10]. However, this by no means implies they are unimportant. In fact, they contribute to the backward radiation and affect the radiation pattern of an antenna made with DNG medium [22]. Complete mode spectrum, including both proper and improper modes, are tabled in this paper. It is desirable to know these spectra when dealing with layered media or discontinuity problems using the mode matching method. Surface wave suppression is also discussed. The sufficient conditions in [23] are loosened to necessary and sufficient conditions.

The paper is organized as follows: in Section 2 the graphical representations of the eigen equations are drawn to show the possible real roots; in Section 3 evanescent surface modes and their dispersion curves are studied; complex surface modes and the Poynting vectors

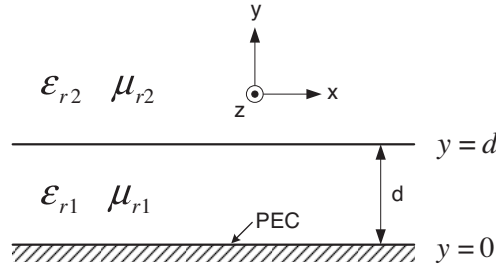


Figure 1. A grounded dielectric slab with lossless, isotropic and homogeneous DNG medium ($\epsilon_{r1} < 0$, $\mu_{r1} < 0$).

as well as the dispersion diagrams including all proper and improper modes are given in Section 4; Section 5 tables the complete mode spectrum; Section 6 discusses the necessary and sufficient conditions to suppress real surface modes; conclusions are drawn in Section 7; proofs on the complex roots loci and the zero power flow are presented in the Appendix.

2. EIGEN EQUATIONS AND GRAPHICAL SOLUTIONS

2.1. Eigen Equations

The structural setup of interest here is a grounded dielectric slab of thickness d (see Fig. 1). Region I is with a DNG medium and region II is air. It is well known that to ensure a positive stored energy in the dielectric layer, passive DNG media must be dispersive and satisfy constraints [7, 25]:

$$\frac{d[\epsilon_r(\omega)\omega]}{d\omega} > 1 \quad \text{and} \quad \frac{d[\mu_r(\omega)\omega]}{d\omega} > 1 \quad (1)$$

where ϵ_r and μ_r are relative permittivity and permeability.

However, the DNG medium considered here is still assumed to be non-dispersive. This assumption is found to be acceptable since a small dispersion of ϵ_r and μ_r can satisfy the inequalities. Furthermore, these limitations can be overcome with active inclusions [17].

Using the transverse resonance method, the eigen equations for TE and TM modes are listed as follows [26]:

$$\frac{\mu_{r1}}{\gamma_{y1}} \tanh(\gamma_{y1}d) + \frac{\mu_{r2}}{\gamma_{y2}} = 0 \quad \text{for TE} \quad (2)$$

$$\frac{\gamma_{y1}}{\epsilon_{r1}} \tanh(\gamma_{y1}d) + \frac{\gamma_{y2}}{\epsilon_{r2}} = 0 \quad \text{for TM} \quad (3)$$

where

$$\begin{aligned}\gamma_{y1}^2 &= -k_0^2 \epsilon_{r1} \mu_{r1} - \gamma^2 \\ \gamma_{y2}^2 &= -k_0^2 \epsilon_{r2} \mu_{r2} - \gamma^2\end{aligned}\quad (4)$$

and $k_0^2 = \omega^2 \mu_0 \epsilon_0$. One should notice in (4) that γ_{y1} and γ_{y2} are complex numbers when the propagation constant in z -direction, $\gamma = \alpha + j\beta$, is a complex number ($\alpha \neq 0$). To solve the equations, γ_{yi} ($i = 1, 2$) has to be written as $\gamma_{yi} = \pm \sqrt{-k_0^2 \epsilon_{ri} \mu_{ri} - \gamma^2}$. The double-valued nature of the square root imposes the branch cut issue. It does not matter which sign γ_{y1} uses since the sign of γ_{y1} outside the hyperbolic tangent cancels with the sign of γ_{y1} inside the hyperbolic tangent as can be seen in (2) and (3). The sign of γ_{y2} , however, does affect the solutions and has significant physical meanings. The electromagnetic fields in the air region bear the form of $e^{-\gamma_{y2}y}$. A proper sign should be chosen to make the real part of γ_{y2} positive to ensure zero fields as $y \rightarrow \infty$. According to the definition of Riemann sheet in [27], this corresponds to a choice of the top Riemann sheet. The solutions lying on the bottom Riemann sheet are non-physical since they have exponentially increasing fields in air. They are usually termed leaky modes and are still found to be useful in applications [28].

2.2. Graphical Method

The graphical method is applied to find real roots. For ordinary surface modes, $\gamma_{y1} = jk_{y1}$ and $\gamma_{y2} = \alpha_{y2}$, where both k_{y1} and α_{y2} are real numbers. The eigen equations (2), (3), and (4) are rewritten as follows:

$$\frac{\mu_{r2}}{\mu_{r1}}(k_{y1}d) \cot(k_{y1}d) = -\alpha_{y2}d \quad \text{for TE} \quad (5)$$

$$\frac{\epsilon_{r2}}{\epsilon_{r1}}(k_{y1}d) \tan(k_{y1}d) = \alpha_{y2}d \quad \text{for TM} \quad (6)$$

$$(k_{y1}d)^2 + (\alpha_{y2}d)^2 = (k_0d)^2(\epsilon_{r1}\mu_{r1} - \epsilon_{r2}\mu_{r2}) \quad (7)$$

The evanescent surface modes have exponentially decaying electromagnetic fields in both air and dielectric layer. Therefore for evanescent surface modes, $\gamma_{y1} = \alpha_{y1}$ and $\gamma_{y2} = \alpha_{y2}$, where both α_{y1} and α_{y2} are real numbers. The eigen equations are rewritten as follows:

$$\frac{\mu_{r2}}{\mu_{r1}}(\alpha_{y1}d) \coth(\alpha_{y1}d) = -\alpha_{y2}d \quad \text{for TE} \quad (8)$$

$$\frac{\epsilon_{r2}}{\epsilon_{r1}}(\alpha_{y1}d) \tanh(\alpha_{y1}d) = -\alpha_{y2}d \quad \text{for TM} \quad (9)$$

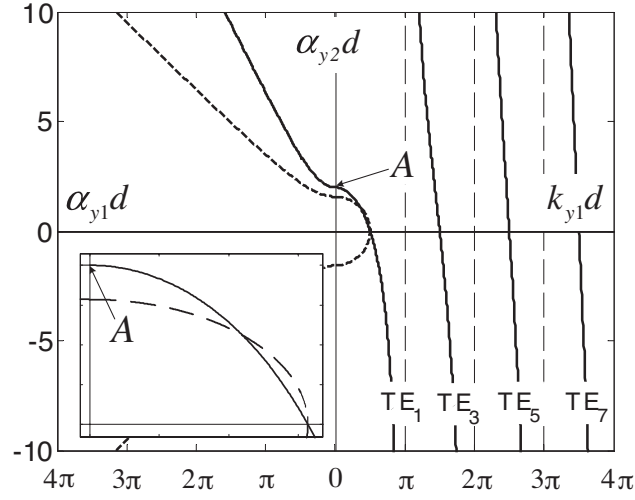
$$(\alpha_{y2}d)^2 - (\alpha_{y1}d)^2 = (k_0d)^2(\epsilon_{r1}\mu_{r1} - \epsilon_{r2}\mu_{r2}) \quad (10)$$

Graphical representations of the above equations are shown in Fig. 2. The index notation here follows [29]: only TE even modes (but with odd indices, TE₁, TE₃, ...) and TM odd modes (but with even indices, TM₀, TM₂, ...) can exist in a grounded dielectric slab. Notice that in the first and second quadrants, α_{y2} is positive and the fields exponentially decay in the air region (proper); in the third and fourth quadrants, α_{y2} is negative and the fields exponentially increase in the air region (improper). The x -axis is divided into two segments. The right half is for $k_{y1}d$, whose fields inside the dielectric layer are sine/cosine standing waves (ordinary), while the left half is for $\alpha_{y1}d$, whose fields inside the dielectric layer are exponentially distributed (evanescent). The intersection in the second quadrant represents the proper evanescent surface mode which does not exist for a DPS medium. This can be seen from (5), (6), (8), and (9): the difference for DPS and DNG media is a minus sign on the left sides of these equations, which implies that one can get results for a DPS medium by reflecting Fig. 2 along its horizontal axis. By doing this, the intersection in the second quadrant will be in the third quadrant which represents an improper mode.

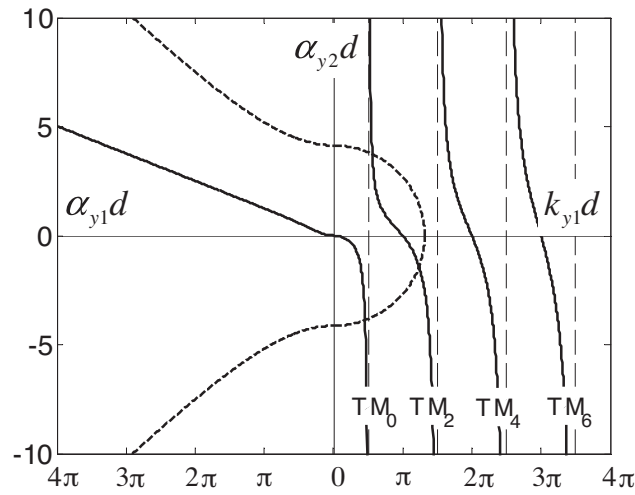
Another important fact that can be seen from Fig. 2 is that the ordinary surface wave solutions for a DNG medium are no longer monotonic. It is clear from the subfigure in the left corner of Fig. 2(a) that there are two intersections as the radius of the dashed circle decreases, which corresponds to a decrease of frequency. Once the circle has only one tangential point with the solid line, further decreasing frequency will cause this mode to be cutoff. Similar occurrence happens to TM modes in Fig. 2(b) in a more obvious way. These two possible modes have two different power distributions. One has more power flowing in the air region than in the dielectric region, making the total power flow in the same direction as the phase velocity. The other is in the opposite way and displays the backward property [30]. More details on the Poynting vectors are addressed in Section 4.

3. EVANESCENT SURFACE MODES

As stated in Section 2, the proper evanescent surface mode does exist with a DNG medium. It is the intersection in the second quadrant. The normalized effective dielectric constant $\epsilon_{eff} = (\beta/k_0)^2$ for evanescent surface mode is larger than $\epsilon_{r1}\mu_{r1}$ and $\epsilon_{r2}\mu_{r2}$. Therefore $\gamma_{y1} = \sqrt{-k_0^2\epsilon_{r1}\mu_{r1} - \gamma^2} = k_0\sqrt{\epsilon_{eff} - \epsilon_{r1}\mu_{r1}}$ is a pure real number. The electromagnetic fields inside the dielectric layer are no longer



(a) TE



(b) TM

Figure 2. Graphical solutions for TE and TM modes. Solid lines in the first and fourth quadrants represent (5) or (6); solid lines in the second quadrant represent (8) or (9); dashed line in the first and fourth quadrants represents (7); dashed line in the second and third quadrants represents (10). The medium parameters are: $\epsilon_{r1} = -2.5$, $\mu_{r1} = -0.5$, $\epsilon_{r2} = 1$, $\mu_{r2} = 1$.

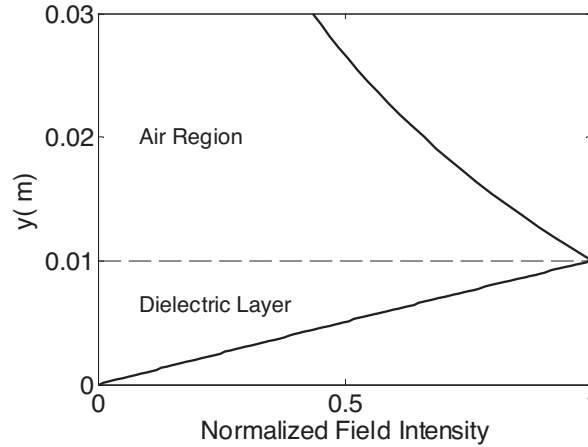


Figure 3. Demonstration of field distribution for TE evanescent surface mode. Medium and structure parameters are: $\epsilon_{r1} = -2.5$, $\mu_{r1} = -2.5$, $\epsilon_{r2} = 1$, $\mu_{r2} = 1$, $d = 0.01$ m, $k_0 = 10$ rad/m. Solved propagation constant: $\gamma/k_0 = j4.27819$.

sine/cosine standing waves, but with the form of $Ae^{-\alpha_y y} + Be^{\alpha_y y}$. Fig. 3 shows a typical field configuration for evanescent surface modes. Notice that the fields extend to the air region far away and decay very slowly.

It is found that the dispersion curves for evanescent surface modes are complicated and highly dependent on the medium parameters. Fig. 4 shows two dispersion diagrams for TE₁ mode with different medium parameters. The curves represent the intersection points of the dashed line and the first solid branch in Fig. 2(a), including the part in the second quadrant. The solid line in Fig. 4 is for proper modes while the dotted line is for improper mode, which is the set of intersections in the fourth quadrant in Fig. 2(a). The dashed lines in both figures depict the value of $\sqrt{\epsilon_{r1}\mu_{r1}}$. They are the watersheds by which one can tell the evanescent surface mode from ordinary ones.

In Fig. 4(a), the evanescent surface mode has low cutoff frequency. As the frequency increases, the ordinary surface mode becomes an evanescent surface mode and its effective dielectric constant, ϵ_{eff} , keeps increasing. In Fig. 4(b), however, the situation is reversed. The evanescent surface mode has a high cutoff frequency above which it becomes the ordinary surface mode. At the low frequency range, the evanescent surface mode has an extremely large ϵ_{eff} that decreases rapidly as the frequency increases. One can refer to the subfigures

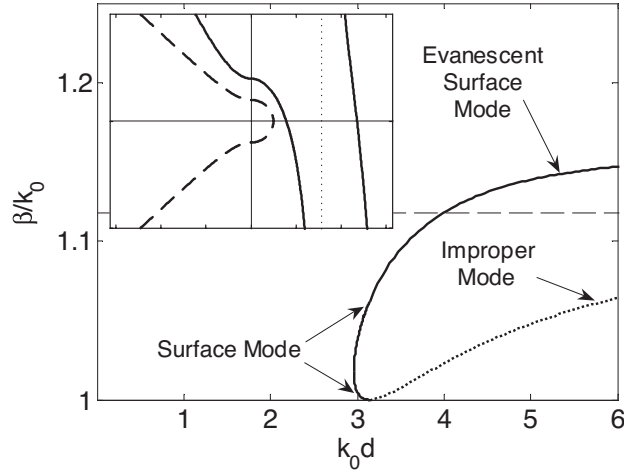
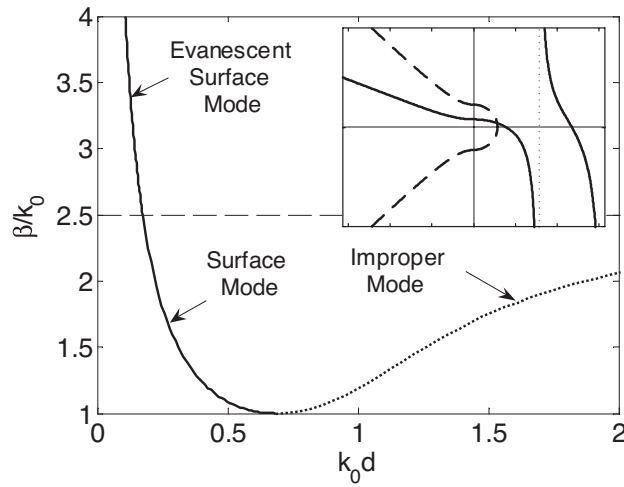
(a) $\epsilon_{r1} = -2.5, \mu_{r1} = -0.5, \epsilon_{r2} = 1, \mu_{r2} = 1$ (b) $T\epsilon_{r1} = -2.5, \mu_{r1} = -2.5, \epsilon_{r2} = 1, \mu_{r2} = 1$

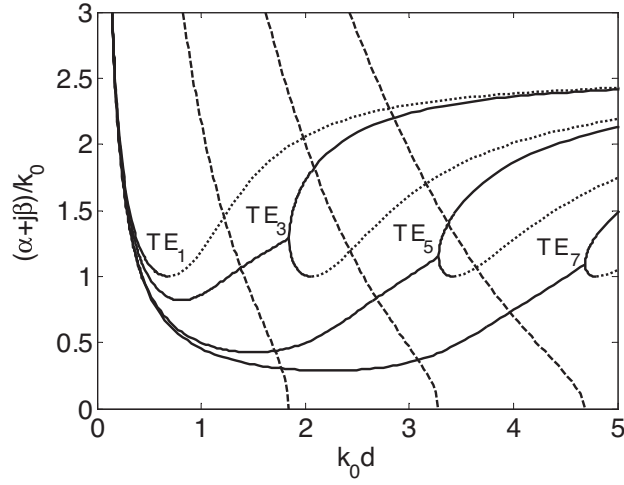
Figure 4. Two possible dispersion curves for TE proper surface modes (solid lines) and TE improper leaky modes (dotted lines). The dashed line, representing $\sqrt{\epsilon_{r1}\mu_{r1}}$, is the watershed for evanescent surface mode and ordinary surface modes.

of Fig. 4 to check the validations. The reason for such significantly different dispersion curves is that with DNG metamaterials, one not only can make ϵ_r and μ_r simultaneously negative but also can let their absolute values be less than unity [19]. From (5) and Fig. 2(a), it is easy to see that the crossing point of the first solid branch TE_1 with the x -axis is fixed at $(\pi/2, 0)$ while the crossing point with the y -axis noted as 'A' in Fig. 2(a) is $(0, |\mu_{r2}/\mu_{r1}|)$. With a conventional DPS medium, μ_{r1} is always equal to unity, or slightly greater or smaller than unity as in the case of paramagnetic or diamagnetic materials. With metamaterials, μ_{r1} is no longer confined near unity and the intercept with the y -axis may change significantly. This change affects the possible intersections of the first solid line and the dashed line in Fig. 2(a) and finally results in dramatically different dispersion curves. By referring to Table 2, it is easy to see that for TE case, $|\mu_{r2}/\mu_{r1}| = 1$ is the critical condition for these two different shapes.

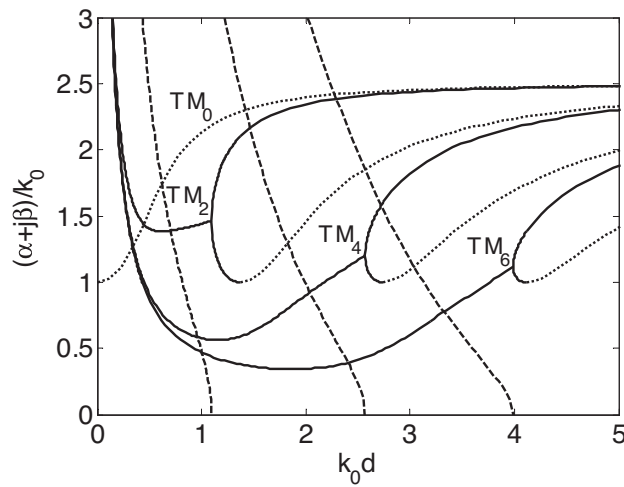
4. COMPLEX SURFACE MODES AND POYNTING VECTORS

It is well known that the complete proper mode spectrum of a DPS dielectric slab include discrete surface modes and continuous radiation modes, both of which are real modes [31, 26]. With a DNG medium, it is proved in Appendix A that all complex roots of the eigen equations are on the top Riemann sheet. These solutions, termed complex surface waves, form another set of proper modes. Unlike real surface modes, complex surface modes have high cutoff frequencies which means that they exist only when the frequency is below the cutoff frequencies. Therefore, there are an infinite number of complex surface modes from very low frequency all the way to high frequency.

Fig. 5 shows dispersion diagrams for both TE and TM modes, including evanescent, ordinary, and complex surface modes. Also included are real improper modes drawn as dotted lines. When the frequency is much lower than the first cutoff frequency of the real modes, all complex modes exist with very high normalized α and β . As the frequency increases, β/k_0 tends to decrease rapidly within a very narrow frequency range followed by a steady increase until its cutoff frequency. Notice that it is not monotonic and the value of β/k_0 can be less than unity, a notable difference compared with real modes. The curve of α/k_0 , however, monotonically decreases very fast as the frequency increases. At the cutoff point, α reaches zero and β becomes the starting point of the real mode. The real surface mode bifurcates into two branches from the cutoff point. One branch has an increasing β/k_0 as the frequency goes high while the other has a decreasing β/k_0 .



(a) TE



(b) TM

Figure 5. Dispersion diagrams for all modes. Solid line is for normalized β of the proper modes. Dashed line is for normalized α of the proper modes. Dotted line is for normalized β of the improper modes. The medium parameters are: $\epsilon_{r1} = -2.5$, $\mu_{r1} = -2.5$, $\epsilon_{r2} = 1$, $\mu_{r2} = 1$.

The branch with an decreasing β/k_0 will reach unity shortly. This property is expected from Fig. 2 and is explained in Section 2. Further increasing frequency makes β/k_0 of the second branch begin to rise. However, it is no longer a proper mode. Notice that the figures are plotted as functions of normalized electrical dimension of the slab, therefore they can be used for inherently dispersive metamaterials, as long as one interprets them as fixed operating frequency while the layer thickness is changing [10].

The existence of an infinite number of complex surface modes at any frequency seems to void the attempt to suppress surface modes since they will carry away power and lower the radiation efficiency. Fortunately, a careful examination on the Poynting vector eliminates this possibility.

To derive the Poynting vector for complex modes, γ_{y1} , γ_{y2} , and γ are assumed to be complex numbers:

$$\begin{aligned}\gamma_{y1} &= p + jq \\ \gamma_{y2} &= u + jv \\ \gamma &= \alpha + j\beta\end{aligned}\quad (11)$$

The Poynting vector for TE modes is written as

$$S_z^{\text{TE}} = \frac{1}{2}E_x H_y^* = \frac{|A|^2}{2} \begin{cases} S_{z1}^{\text{TE}}, & \text{for } 0 < y < d \\ S_{z2}^{\text{TE}}, & \text{for } y \geq d \end{cases} \quad (12)$$

where A is the field intensity and S_{z1}^{TE} and S_{z2}^{TE} are as follows:

$$S_{z1}^{\text{TE}}(y, z) = \frac{\beta + j\alpha}{2\omega\mu_{r1}} e^{-2\alpha z} [\cosh(2py) - \cos(2qy)] \quad (13)$$

$$S_{z2}^{\text{TE}}(y, z) = \frac{\beta + j\alpha}{2\omega\mu_{r2}} e^{-2u(y-d) - 2\alpha z} [\cosh(2pd) - \cos(2qd)] \quad (14)$$

The total power flow in z -direction:

$$\begin{aligned}P_z^{\text{TE}}(z) &= \int_0^d \text{Re} [S_{z1}^{\text{TE}}(y, z)] dy + \int_d^\infty \text{Re} [S_{z2}^{\text{TE}}(y, z)] dy \\ &= \frac{\beta e^{-2\alpha z}}{4\omega\mu_{r1}} \left[\frac{\sinh(2pd)}{p} - \frac{\sin(2qd)}{q} \right] \\ &\quad + \frac{\beta e^{-2\alpha z}}{4\omega\mu_{r2}} \left[\frac{\cosh(2pd)}{u} - \frac{\cos(2qd)}{u} \right]\end{aligned}\quad (15)$$

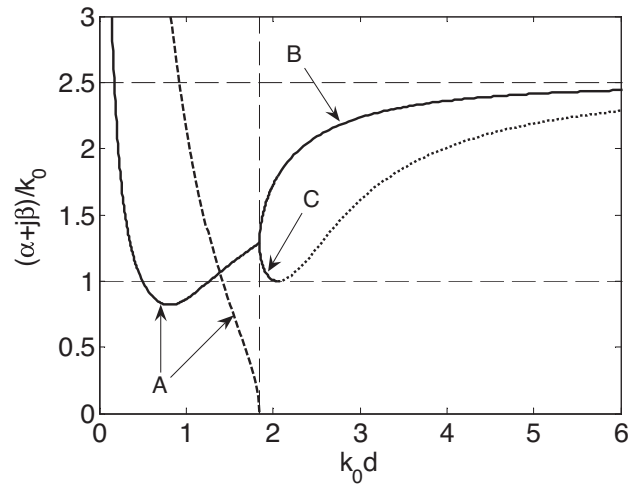
Although the above equation of the total power flow is quite complicated, the result turns out to be simply zero [10]. The detailed

proof is given in Appendix B. Fig. 6 shows the dispersion diagram and the Poynting vector for the TE_3 mode. In Fig. 6(a), only the complex mode exists (branch ‘A’) when the frequency is lower than the cutoff frequency. The zero power flow in Fig. 6(b) shows that the complex surface mode does not carry away power in z -direction. As the frequency increases, two real surface modes appear from the cutoff point. The top branch (branch ‘B’) carries a negative power flow and has backward properties. When a waveguide operates at this mode, its fields are largely confined inside the dielectric layer. The bottom branch (branch ‘C’) carries a positive power flow and its fields extend far away in the air region. Further increasing frequency causes the fields in the air region to decay more slowly and eventually will reach infinity. At that point, the radiation boundary conditions are violated and the mode becomes improper.

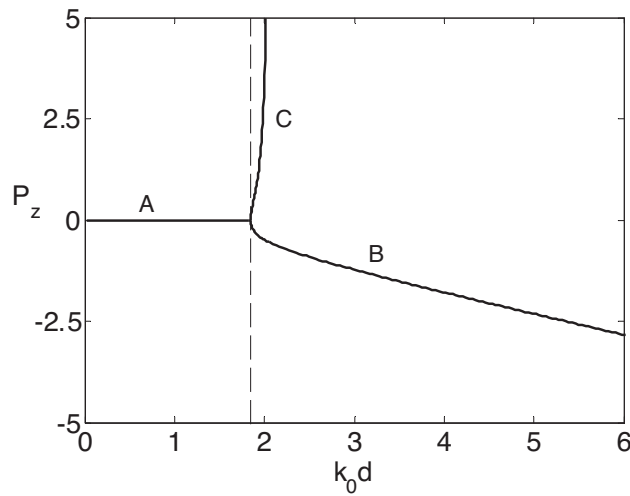
To give out a clear picture of the power flow density, the Poynting vector is drawn in Fig. 7. Dotted lines are the boundaries of a conjectured box with dimension of $4\text{ mm} \times 20\text{ mm}$. The power flow has different directions in the air and inside the dielectric layer. The average total power flowing out of the box via the left and right side walls is equal to the power flowing into the box from the top wall. Now assuming the top wall is moved to infinity, there is no power flowing into the box from the top wall since the complex surface modes have zero fields at infinity. According to the energy conservation law, the power exchange via the left side wall $P_1 = \int_0^\infty S_z(y, z_1) dy$ must be equal to the power exchange via the right side wall $P_2 = \int_0^\infty S_z(y, z_2) dy$. Note that the propagation constant along z -direction is now a complex number $\gamma = \alpha + j\beta$ where $\alpha \neq 0$, and P_1 and P_2 are related by $P_2 = P_1 e^{-2\alpha(z_2 - z_1)}$. To ensure $P_1 = P_2$, the only possibility is $P_1 = P_2 = 0$. Thus all the complex surface modes have zero power flow in the z -direction. They do not transport any energy. [32], [33] got similar conclusions, but both of them are for bounded structure.

5. COMPLETE MODE SPECTRUM OF DIELECTRIC SLAB

Based on the discussion above and the proof in Appendix A, complete mode spectrum for dielectric slab are ready to be made. Table 1 lists proper and improper modes for both DPS and DNG media. Notice that the infinite number of complex modes now belong to the proper spectrum for a DNG medium. One cannot ignore these modes, but it is also unnecessary to pay attention on all of them. From Fig. 5, it is seen that within a narrow frequency band only several complex surface modes are important and the others vanish either because they



(a) Dispersion diagram



(b) Power flow in z -direction

Figure 6. Dispersion diagram and the power flow in z -direction for TE_3 modes shown in Fig. 5(a). ‘A’ is for the complex surface mode; ‘B’ is for top branch of the real surface mode; ‘C’ is for bottom branch of the real surface mode. The medium parameters are: $\epsilon_{r1} = -2.5$, $\mu_{r1} = -2.5$, $\epsilon_{r2} = 1$, $\mu_{r2} = 1$.

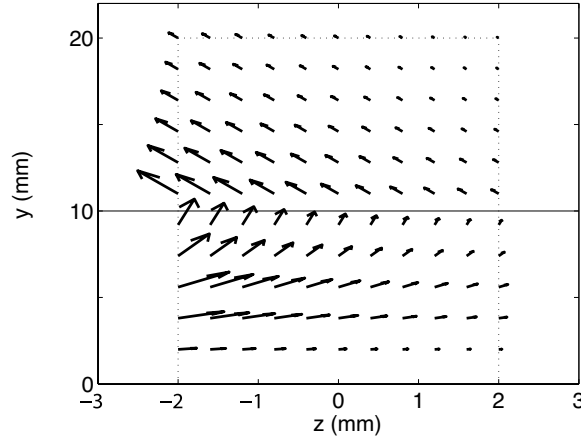


Figure 7. The Poynting vector of a TE complex mode. Dotted lines is the boundary of a conjectured box. Solid line is the boundary of the dielectric slab and the air. The medium and structure parameters are: $\epsilon_{r1} = -2.5$, $\mu_{r1} = -2.5$, $\epsilon_{r2} = 1$, $\mu_{r2} = 1$, $d = 0.01$ m, $k_0 = 100$ rad/m. Solved propagation constant: $\gamma/k_0 = 2.09195 - j0.86938$.

are already beyond cutoff or because their high α/k_0 keep them trivial. Notice that both the DPS and DNG media have proper and improper ordinary real modes. They are the intersections in the first and the fourth quadrants in Fig. 2.

Table 1. Complete mode spectrum for dielectric slab.

Spectrum	DPS	DNG
Discrete evanescent real mode $\alpha = 0, \beta/k_0 > \sqrt{\epsilon_{r1}\mu_{r1}}$	Improper	Proper
Discrete ordinary real mode $\alpha = 0, \sqrt{\epsilon_{r2}\mu_{r2}} < \beta/k_0 < \sqrt{\epsilon_{r1}\mu_{r1}}$	Proper/Improper	Proper/Improper
Continuous radiation mode $\alpha = 0, \beta/k_0 < \sqrt{\epsilon_{r2}\mu_{r2}}$	Proper	Proper
Discrete complex mode $\alpha \neq 0, \beta \neq 0$	Improper	Proper

6. SURFACE WAVE SUPPRESSION

It is well known that the dielectric slab with a DPS medium has no cutoff frequency for TM_0 modes. For a DNG medium, both TE and TM real modes have cutoff frequencies as shown in Fig. 2. Based on this foundation, P. Baccarelli and his colleagues suggested the concept of surface wave suppression. However, most conditions given in [24] are sufficient conditions. To give designers more freedom, necessary and sufficient conditions are given in Tables 2 and 3.

Table 2. Necessary and sufficient conditions for TE surface-wave suppression. The dielectric constants for the air region are assumed to be $\epsilon_{r2} = 1, \mu_{r2} = 1$ and thus are omitted. ‘Ord.’ stands for ordinary surface modes and ‘Eva.’ stands for evanescent surface modes. $a = k_0 d \sqrt{\epsilon_{r1} \mu_{r1} - 1}$ is for $\epsilon_{r1} \mu_{r1} > 1$, while $b = k_0 d \sqrt{1 - \epsilon_{r1} \mu_{r1}}$ is for $\epsilon_{r1} \mu_{r1} < 1$.

	$\epsilon_{r1} \mu_{r1} < 1$	$\epsilon_{r1} \mu_{r1} > 1$
Ord.	-	$a < \min_{0 \leq x \leq \pi/2} \left\{ x \sqrt{1 + \frac{\cot^2 x}{\mu_{r1}^2}} \right\}$ or $\max_{0 \leq x \leq \pi/2} \left\{ x \sqrt{1 + \frac{\cot^2 x}{\mu_{r1}^2}} \right\} < a < \min_{\pi \leq x \leq 3\pi/2} \left\{ x \sqrt{1 + \frac{\cot^2 x}{\mu_{r1}^2}} \right\}$
Eva.	$ \mu_{r1} < 1$	$\begin{cases} \mu_{r1} > 1 \\ a > \frac{1}{ \mu_{r1} } \end{cases}$ or $\begin{cases} \mu_{r1} < 1 \\ a < \min_{0 \leq x \leq (1 - \mu_{r1}^2)^{-1/2}} \left\{ x \sqrt{\frac{\coth^2 x}{\mu_{r1}^2} - 1} \right\} \end{cases}$

As an example to demonstrate the procedure of deriving these conditions, consider TE ordinary surface modes. From Fig. 2(a), it is quite straightforward that the conditions must ensure no intersection between the dashed circle and the solid lines in the first quadrant. The radius of the dashed circle given by (7) is $a = k_0 d \sqrt{\epsilon_{r1} \mu_{r1} - \epsilon_{r2} \mu_{r2}}$. The minimum and maximum distances from the origin to the first solid branch are assumed to be s_1 and s_2 . The minimum distance from the origin to the second solid branch is assumed to be s_3 . Then it is clear

Table 3. Necessary and sufficient conditions for TM surface-wave suppression. Others are the same as Table 2.

	$\epsilon_{r1}\mu_{r1} < 1$	$\epsilon_{r1}\mu_{r1} > 1$
Ord.	-	$a < \min_{\pi/2 \leq x \leq \pi} \left\{ x \sqrt{1 + \frac{\tan^2 x}{\epsilon_{r1}^2}} \right\}$
Eva.	$ \epsilon_{r1} \leq 1$ and $b > \max_{0 \leq x \leq \tanh^{-1} \epsilon_{r1} } \left\{ x \sqrt{1 - \frac{\tanh^2 x}{\epsilon_{r1}^2}} \right\}$	$ \epsilon_{r1} > 1$

that the condition of suppressing TE ordinary surface modes is $a < s_1$ or $s_2 < a < s_3$. The detailed formulae are:

$$a < \min_{0 \leq x \leq \pi/2} \left\{ x \sqrt{1 + \frac{\cot^2 x}{\mu_{r1}^2}} \right\} \quad (16)$$

or

$$\max_{0 \leq x \leq \pi/2} \left\{ x \sqrt{1 + \frac{\cot^2 x}{\mu_{r1}^2}} \right\} < a < \min_{\pi \leq x \leq 3\pi/2} \left\{ x \sqrt{1 + \frac{\cot^2 x}{\mu_{r1}^2}} \right\} \quad (17)$$

Notice that for the sake of simplicity the dielectric constants for the air region are assumed to be $\epsilon_{r2} = \mu_{r2} = 1$, thus, they are omitted. Using the same procedure, necessary and sufficient conditions for other modes can be derived.

7. CONCLUSIONS

In this paper, an investigation on the mode properties of a grounded dielectric slab with a DNG medium has been dealt with the aims of getting complete spectrum and the necessary and sufficient conditions for surface wave suppression.

The graphical method is applied to solve the eigen equations for real roots. Different shapes of dispersion curves for evanescent surface modes show that they are very sensitive to material parameters. The complex modes are proved to be exclusively proper and have zero power flow. They do not carry away energy in both transverse and longitudinal directions. Complete mode spectra are tabled for both DPS and DNG media. The sufficient conditions for surface wave suppression are loosened to necessary and sufficient conditions.

Although the considered medium is idealized and currently cannot be realized, the results of this paper still unveil some exotic properties as well as potential applications of the metamaterials.

APPENDIX A. PROOF OF THE PROPER COMPLEX MODES

Equation (2) to (4) listed in Section II are used to find eigen value $\gamma = \alpha + j\beta$. (2) and (3) are transcendental equations and have complex roots even with lossless medium. Using the similar procedure in [26], we will prove that all complex roots with DNG medium are located on the top Riemann sheet. The TM case is used as example, but the proof procedure as well as the conclusion are applied to the TE case in exactly the same way.

With $\epsilon_r = \epsilon_{r1}/\epsilon_{r2}$, (3) is rewritten as:

$$-\epsilon_r \gamma_{y2} = \gamma_{y1} \tanh(\gamma_{y1}d) \quad (\text{A1})$$

By using (11) and letting the real part and imaginary part of each side of (A1) be equal (assuming ϵ_r is a real number), one gets [26]:

$$u = -\frac{1}{\epsilon_r} \frac{p \sinh(2pd) - q \sin(2qd)}{\cosh(2pd) + \cos(2qd)} \quad (\text{A2})$$

$$v = -\frac{1}{\epsilon_r} \frac{q \sinh(2pd) + p \sin(2qd)}{\cosh(2pd) + \cos(2qd)} \quad (\text{A3})$$

Substituting (11) into (4), one gets another two equations:

$$u^2 - v^2 = p^2 - q^2 + k_0^2(\epsilon_{r1}\mu_{r1} - \epsilon_{r2}\mu_{r2}) \quad (\text{A4})$$

$$uv = pq \quad (\text{A5})$$

Now we have four equations, (A2) to (A5), and four unknowns, p , q , u , and v . Notice that changing p to $-p$, or q to $-q$, or both does not change the validation of these four equations [26, 21]. Based on this observation, we confine our discussion to the first quadrant of the γ_{y1} plane, or positive p and positive q .

For DNG media $\epsilon_r < 0$, if u is negative, from (A2) one has $q \sin(2qd) > p \sinh(2pd)$. To ensure (A5), v must be negative as well since both p and q are positive. According to (A3), $q \sinh(2pd) + p \sin(2qd) < 0$. Thus one gets two conditions which contradict each other:

$$\sin(2qd) > \frac{p \sinh(2pd)}{q} > 0 \quad (\text{A6})$$

$$-\sin(2qd) > \frac{q \sinh(2pd)}{p} > 0 \quad (\text{A7})$$

We then prove that for DNG media u is always positive and all complex roots are on the top Riemann sheet.

APPENDIX B. PROOF OF ZERO POWER FLOW

Based on the proof in Appendix I, it is easy to see that the proper complex modes have zero power flow in z -direction. Similar conclusions were given for plasma layer [34] and for improper leaky modes in open and closed waveguides [35].

The Poynting vector in z -direction for complex TM modes is:

$$S_z^{\text{TM}} = -\frac{1}{2}E_y H_x^* = \frac{|A|^2}{2} \begin{cases} S_{z1}^{\text{TM}}, & \text{for } 0 < y < d \\ S_{z2}^{\text{TM}}, & \text{for } y \geq d \end{cases} \quad (\text{B1})$$

where A is the field intensity and S_{z1}^{TM} and S_{z2}^{TM} are as follows:

$$S_{z1}^{\text{TM}}(y, z) = \frac{\beta - j\alpha}{2\omega\epsilon_{r1}} e^{-2\alpha z} [\cosh(2py) + \cos(2qy)] \quad (\text{B2})$$

$$S_{z2}^{\text{TM}}(y, z) = \frac{\beta - j\alpha}{2\omega\epsilon_{r2}} e^{-2u(y-d) - 2\alpha z} [\cosh(2pd) + \cos(2qd)] \quad (\text{B3})$$

The power flow in z -direction of region 1 is:

$$\begin{aligned} P_{z1}^{\text{TM}}(z) &= \int_0^d S_{z1}^{\text{TM}}(y, z) dy \\ &= \frac{\beta - j\alpha}{4\omega\epsilon_{r1}} e^{-2\alpha z} \left[\frac{q \sinh(2pd) + p \sin(2qd)}{pq} \right] \\ &= \frac{\beta - j\alpha}{4\omega\epsilon_{r1}} e^{-2\alpha z} \left[-\epsilon_r v \frac{\cosh(2pd) + \cos(2qd)}{pq} \right] \\ &= -\frac{\beta - j\alpha}{4\omega} e^{-2\alpha z} \left[\frac{\cosh(2pd) + \cos(2qd)}{u\epsilon_{r2}} \right] \end{aligned} \quad (\text{B4})$$

In the above derivation, (A3) and (A5) have been used.

The power flow in z -direction of region 2 is:

$$\begin{aligned} P_{z2}^{\text{TM}}(z) &= \int_d^\infty S_{z2}^{\text{TM}}(y, z) dy \\ &= \frac{\beta - j\alpha}{4\omega} e^{-2\alpha z} \left[\frac{\cosh(2pd) + \cos(2qd)}{u\epsilon_{r2}} \right] \end{aligned} \quad (\text{B5})$$

And the total power flow in z -direction is:

$$P_z^{\text{TM}}(z) = P_{z1}^{\text{TM}}(z) + P_{z2}^{\text{TM}}(z) = 0 \quad (\text{B6})$$

REFERENCES

1. Vesalago, V. G., "The electrodynamics of substances with simultaneously negative values of ϵ and μ ," *Soviet Physics USPEKI*, Vol. 10, 509–514, 1968.
2. Pendry, J. B., A. J. Holden, W. J. Stewart, and I. Youngs, "Extremely low frequency plasmons in metallic mesostructures," *Phys. Rev. Lett.*, Vol. 76, 4773–4776, June 1996.
3. Pendry, J. B., A. J. Holden, D. J. Robbins, and W. J. Stewart, "Magnetism from conductors and enhanced nonlinear phenomena," *IEEE Trans. Microwave Theory Tech.*, Vol. 47, 2075–2084, Nov. 1999.
4. Pendry, J. B., "Negative refraction makes a perfect lens," *Phys. Rev. Lett.*, Vol. 85, 3966–3969, Oct. 2000.
5. Smith, D. R., W. J. Padilla, D. C. Vier, S. C. Nemat-Nasser, and S. Schultz, "Composite medium with simultaneously negative permeability and permittivity," *Phys. Rev. Lett.*, Vol. 84, 4184–4187, May 2000.
6. Shelby, R. A., D. R. Smith, and S. Schultz, "Experimental verification of a negative index of refraction," *Science*, Vol. 292, 72–79, Apr. 2001.
7. Smith, D. R. and N. Kroll, "Negative refractive index in left-handed materials," *Phys. Rev. Lett.*, Vol. 85, 2933–2936, Oct. 2000.
8. Markos, P. and C. M. Soukoulis, "Numerical studies of left-handed materials and arrays of split ring resonators," *Phys. Rev. E*, Vol. 65, 036622, Mar. 2002.
9. Alù, A. and N. Engheta, "Pairing an epsilon-negative slab with a mu-negative slab: resonance, tunneling and transparency," *IEEE Trans. Microwave Theory Tech.*, Vol. 51, 2558–2571, Oct. 2003.
10. Alù, A. and N. Engheta, "An overview of salient properties of planar guided-wave structures with double-negative (DNG) and single-negative (SNG) layers," *Negative-Refraction Metamaterials: Fundamental Principles and Applications*, G. V. Eleftheriades and K. G. Balmain (eds.), 339–380, John Wiley & Sons, New Jersey, 2005.
11. Caloz, C. and T. Itoh, "Transmission line approach of left-handed (LH) materials and microstrip implementation of an artificial LH transmission line," *IEEE Trans. Microwave Theory Tech.*, Vol. 52, 1159–1166, May 2004.
12. Lin, I.-H., M. DeVincentis, C. Caloz, and T. Itoh, "Arbitrary dual-

- band components using composite right/left-handed transmission lines,” *IEEE Trans. Microwave Theory Tech.*, Vol. 52, 1142–1149, Apr. 2004.
13. Mittra, R., K. Rajab, and M. T. Lanagan, “Size reduction of microstrip antennas using metamaterials,” *Proc. IEEE AP-S*, Washington, DC, July 2005.
 14. Erentok, A. and R. W. Ziolkowski, “Development of epsilon-negative (ENG) metamaterials for efficient electrically small antenna applications,” *Proc. IEEE AP-S*, Washington, DC, July 2005.
 15. Cory, H. and A. Barger, “Surface-wave propagation along a metamaterial slab,” *Microwave Opt. Technol. Lett.*, Vol. 38, 392–395, Sept. 2003.
 16. Dong, H. and T. X. Wu, “Analysis of discontinuities in double-negative (DNG) slab waveguides,” *Microwave Opt. Technol. Lett.*, Vol. 39, 483–488, Dec. 2003.
 17. Nefedov, I. S. and S. A. Tretyakov, “Waveguide containing a backward-wave slab,” *Radio Sci.*, Vol. 38, 1101–1109, 2003.
 18. Wu, B.-I., T. M. Grzegorzczak, Y. Zhang, and J. A. Kong, “Guided modes with imaginary transverse wave number in a slab waveguide with negative permittivity and permeability,” *J. Appl. Phys.*, Vol. 93, 9386–9388, Jun. 2003.
 19. Shadrivov, I. W., A. A. Sukhorukov, and Y. S. Kivshar, “Guided modes in negative-refractive-index waveguides,” *Phys. Rev. E*, Vol. 67, 057602, May 2003.
 20. Suwailam, M. M. B. and Z. D. Chen, “Surface waves on a grounded double-negative (DNG) slab waveguide,” *Microwave Opt. Technol. Lett.*, Vol. 44, 494–498, Mar. 2005.
 21. Li, C., Q. Sui, and F. Li, “Complex guided wave solutions of grounded dielectric slab made of metamaterials,” *Progress In Electromagnetics Research*, PIER 51, 187–195, 2005.
 22. Baccarelli, P., P. Burghignoli, F. Frezza, A. Galli, P. Lampariello, G. Lovat, and S. Paulotto, “Effects of leaky-wave propagation in metamaterial grounded slabs excited by a dipole source,” *IEEE Trans. Microwave Theory Tech.*, Vol. 53, 32–44, Jan. 2005.
 23. Baccarelli, P. P., Burghignoli, G. Lovat, and S. Paulotto, “Surface-wave suppression in a double-negative metamaterial grounded slab,” *IEEE Antennas Wireless Propag. Lett.*, Vol. 2, 269–272, 2003.
 24. Baccarelli, P., P. Burghignoli, F. Frezza, A. Galli, P. Lampariello, G. Lovat, and S. Paulotto, “Fundamental modal properties

- of surface waves on metamaterial grounded slabs,” *IEEE Trans. Microwave Theory Tech.*, Vol. 53, 1431–1442, Apr. 2005.
25. Landau, L., E. Lifshitz, and L. Pitaevskii, *Electrodynamics of Continuous Media*, 2nd edition, Butterworth-Heinemann, Oxford, England, 1984.
 26. Collin, R. E., *Field Theory of Guided Waves*, 2nd edition, IEEE Press, Piscataway, NJ, 1991.
 27. Chew, W. C., *Waves and Fields in Inhomogeneous Media*, Van Nostrand Reinhold, New York, 1990.
 28. Oliner, A. A., “Leakage from higher modes on microstrip line with applications to antennas,” *Radio Sci.*, Vol. 22, 907–912, 1987.
 29. Balanis, C. A., *Advanced Engineering Electromagnetics*, John Wiley & Sons, NJ, 1989.
 30. Mahmoud, S. F. and A. J. Viitanen, “Surface wave character on a slab of metamaterial with negative permittivity and permeability,” *Progress In Electromagnetics Research*, PIER 51, 127–137, 2005.
 31. Hanson, G. W. and A. B. Yakovlev, *Operator Theory for Electromagnetics*, Springer, NY, 2002.
 32. Rozzi, T., L. Pierantoni, and M. Farina, “General constraints on the propagation of complex waves in closed lossless isotropic waveguides,” *IEEE Trans. Microwave Theory Tech.*, Vol. 46, 512–516, May 1998.
 33. Freire, M. J., F. Mesa, and M. Horno, “Power characteristics of complex modes in both reciprocal and nonreciprocal boxed microstrip lines,” *Microwave Opt. Technol. Lett.*, Vol. 18, 389–394, Aug. 1998.
 34. Tamir, T. and A. A. Oliner, “The spectrum of electromagnetic waves guided by a plasma layer,” *Proceedings of the IEEE*, Vol. 51, 317–332, Feb. 1963.
 35. Laxpati, S. R. and R. Mittra, “Energy considerations in open and closed waveguides,” *IEEE Trans. Antenna and Propag.*, Vol. 18, 883–890, Nov. 1965.